Journal of Biomechanics 117 (2021) 110263

Contents lists available at ScienceDirect

Journal of Biomechanics

journal homepage: www.elsevier.com/locate/jbiomech
www.JBiomech.com

Numerical-experimental analysis of the permeability-porosity relationship in triply periodic minimal surfaces scaffolds

Tiago Pires [a], Jorge Santos [a], Rui B. Ruben [b], Bárbara P. Gouveia [a], André P.G. Castro [a,*], Paulo R. Fernandes [a]

[a] IDMEC, Instituto Superior Técnico, Universidade de Lisboa, Lisbon, Portugal
[b] ESTG, CDRSP, Polytechnic Institute of Leiria, Leiria, Portugal

ARTICLE INFO

Article history:
Accepted 10 January 2021

Keywords:
Bone tissue engineering
Scaffolds
Permeability
Triply periodic minimal surfaces
Computational fluid dynamics

ABSTRACT

Bone Tissue Engineering has been focusing on improving the current methods for bone repair, being the use of scaffolds presented as an upgrade to traditional surgery techniques. Scaffolds are artificially porous matrices, meant to promote cell seeding and proliferation, being these properties influenced by the permeability of the structure. This work employed experimental pressure drop tests and Computational Fluid Dynamics models to assess permeability (and fluid streamlines) within different triply periodic minimal surfaces scaffold geometries (Schwarz D, Gyroid and Schwarz P). The pressure outputs from the computational analysis presented a good correlation with the experimental results, with R^2 equal to 0.903; they have also shown that a lower porosity may not mean a lower permeability if the geometry is altered, such as the difference between 60% porous Gyroid scaffolds ($8.1*10^{-9}$ mm^2) and 70% porous Schwarz D scaffolds ($7.1*10^{-9}$ mm^2). Fluid streamlines revealed how the Gyroid geometries are the most appropriate design for most bone tissue engineering applications, due to their consistent fluid permeation, followed by Schwarz D. The Schwarz P geometries have shown flat streamlines and significant variation of the permeability with the porosity (an increase of 10% in their porosity lead to an increase in the permeability from $5.1*10^{-9}$ mm^2 to $11.7*10^{-9}$ mm^2), which would imply a poor environment for cell seeding and proliferation.

1. Introduction

In bone Tissue Engineering (BTE), the development of scaffolds has been a major area of research (Hollister et al., 2015). This is because scaffolds are porous structures that support cell seeding, cell proliferation, cell differentiation and vascularisation (Coelho et al., 2015; Szklanny et al., 2019). Because of their characteristics, these structures offer an appealing alternative for treating bone injury/defect when compared to bone grafting, which possesses a higher risk of inflammation and immune response to the graft (Porter et al., 2009). Scaffold geometry plays a key role on allowing cells to proliferate inside them (Melchels et al., 2011, 2010), along with determining the osteogenic differentiation of the seeded cells (Castro and Lacroix, 2018; Webber et al., 2015). As discussed by Castro and Lacroix (2018), it is possible to predict what the cells will differentiate into, based on the fluid flow velocity and the shear strain. Both of these factors are influenced by a fundamental characteristic of any scaffold, its permeability (Daish et al., 2019; Nasrollahzadeh and Pioletti, 2016; Rahbari et al., 2017).

Permeability is the measurement of the ability of a porous medium to allow the passage of fluid (usually expressed in m^2). This parameter is crucial in allowing sufficient fluid flow to pass through the scaffold to allow for cell passage. It also affects the preceding cell proliferation and vascularisation. Permeability of a scaffold, like it has been shown in previous studies (Castro et al., 2019a; Dias et al., 2012), is determined by two main factors of its design, the chosen geometry and its porosity. If scaffolds with the same porosity have different architectures, namely different surface areas, their permeability will be different (Castro et al., 2019a) and the same goes for scaffolds that have the same type of geometry but different porosity (Dias et al., 2012), as described by empirically-based permeability measures as the Kozeny-carmen relation (Montazerian et al., 2017)

The triply periodic minimal surfaces (TPMS) method is one of the most discussed design strategies for BTE scaffolds (Giannitelli et al., 2014; Kapfer et al., 2011; Yoo, 2012). TPMS geometries have high surface-to-volume ratio, enhanced pore connectivity and translational symmetry in three independent directions (x, y and z directions), hence being fully controllable for porosity and

* Corresponding author at: IDMEC, Instituto Superior Técnico, Av. Rovisco Pais, 1, 1049-001 Lisbon, Portugal.
E-mail address: andre.castro@tecnico.ulisboa.pt (A.P.G. Castro).

https://doi.org/10.1016/j.jbiomech.2021.110263
0021-9290/

subsequently for stiffness in biomedical applications (Kelly et al., 2017; Maskery et al., 2018; Shi et al., 2018).

This study is focused on analysing the permeability-geometry relation of TPMS scaffolds, through the combination of Computational Fluid Dynamics (CFD) simulations and experimental permeability tests, towards establishing a reliable method for TPMS scaffold design, test and production. Montazerian et al. (2017) conducted a related permeability study regarding TPMS scaffolds with different porosities, but this group has studied the scaffold's normalized permeability instead of the measured permeability. Plus, scaffolds were produced based on their geometry and only their porosity was measured, invalidating the possibility of determining, for a given porosity, which is the more permeable geometry. In terms of the comparing experimental and numerical data, the permeability study by Dias et al. (2012) showed that it is possible to correlate calculated and measured permeability in BTE scaffolds, although the calculated permeability values were approximately four times higher than the measured ones; roughness and wettability surface effects of the materials were among the possible explanations for such differences, but these factors are still difficult to capture numerically (Ali and Sen, 2018a).

Thus, the method proposed here combines the analysis of the fluid streamlines on the numerical models with the experimental permeability calculation, in order to evaluate the differences caused by the scaffold geometry and internal curvature on the fluid permeation. This allows for scaffold selection as a function of the structural configuration of the future host tissue.

2. Materials and methods

For this study, three different TPMS geometries were studied: Schwartz D (SD), Gyroid (SG) and Schwartz P (SP). For each of these geometries, two levels of porosity were implemented (60% and 70%). In total, six architectures were designed that will henceforth be referred in accordance to their geometry and porosity (for example a Gyroid shape with 60% porosity will be referred to as SG60).

These geometries were created as a Finite Element (FE) mesh of the basic cubic unit of the selected scaffold geometry, as a function of its porosity and number of hexahedral elements per cube side. This basic unit is then repeated according to the desired final configuration (Castro et al., 2019b). For this work, the final FE mesh was a 4 × 4 × 4 configuration with 3.25 mm sides, which corresponds to the 13 mm required by the experimental setup. Each basic cubic unit was created with 40 hexahedral elements per side. These FE models were used as input for both 3D printing of the samples (Fig. 1) and CFD simulations.

2.1. Experimental setup

The scaffolds were manufactured using the MJP 3600® MultiJet printer (3D Systems, Rock Hill, SC, USA) and the commercial material Visijet M3 Crystal (recommended by the printer's manufacturer) (3D Systems, 2017). For each of the six tested designs, ten samples were produced. The production process has been previously validated with microCT analysis (Castro et al., 2019b). The experimental setup consisted on a syringe pump for controlled constant flow; a permeability chamber for the scaffold and a pressure transducer that measures the pressure difference before and after the chamber, according to what was previously described in Castro et al. (2019a) and Santos et al. (2020). To ensure consistency across all tests, the entire system was purged of all air after placing each new scaffold. For each scaffold a total of five different flow rates were tested between 5 and 60 ml/min (Chen et al., 2016), with three pressure measurements being taken for each flow rate. This wide range in flow rates was chosen due to the pressure transducer's most adequate working range and inherent lower precision at lower flow rates (Santos et al., 2020).

2.2. Computational modelling and simulation

For the numerical component of the study, the CFD analysis was conducted using FLUENT® ANSYS® (Ansys Inc., Canonsburg, Pennsylvania, USA). This program has already proven to be a useful tool in the study of the fluid flow inside BTE scaffolds (Ali and Sen, 2018b; Campos Marin et al., 2017, 2016). The geometry required for the CFD simulation is that of the inverse of the scaffold, as the purpose is to analyse the fluid flow within the scaffold.

From a computational cost perspective, it was not feasible to represent the entire

13 mm sided cubic scaffold. Therefore, less demanding alternative models were utilised for each scaffold. These numerical models had a 1 × 1 × 4 cubic unit configuration, with the fluid flow following the z direction (from positive to negative). In the × and y directions of the simulations, a periodic boundary condition was applied (which assumes the flow across two opposite planes are identical) creating an infinite structure in both directions (Fig. 2a). These models were made of cubic hexahedral elements (0.08125 mm sided) with a cross section of 3.25 mm × 3.25 mm and a total length of 77 mm (13 mm for the scaffold plus 32 mm for each end of the permeability chamber). A no slip wall condition was considered, alongside a zero pressure outlet (Egan et al., 2017; Zhianmanesh et al., 2019); inlet flow rates ranging from 1 to 60 ml/min (extending the experimental range to lower flow rates) and the occurrence of a laminar flow inside the permeability chamber. The simulations returned the pressure drop at the ends of the models.

The main limitation of the periodic models is the fact that it considers scaffolds with infinite length in the × and y direction, meaning that it does not consider the effect of the chamber walls in the pressure drop. To address this, a second model was created using the symmetric boundary condition. These new models had a 2 × 2 × 4 cubic unit configuration (Fig. 2b), with a symmetry boundary condition on two perpendicular chamber walls, with the remaining having no slip wall boundaries. However, this model

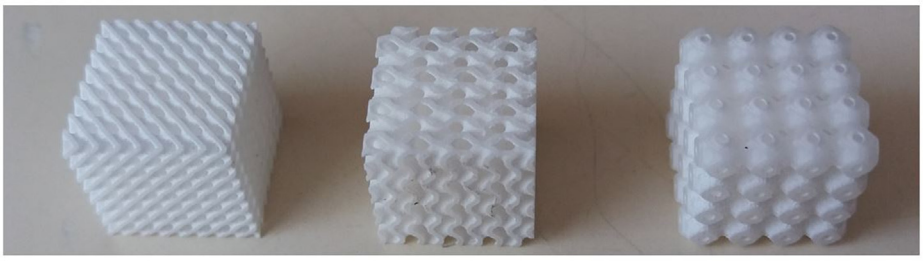

Fig. 1. Example of a 3D printed SD60, SG60 and SP60 scaffolds.

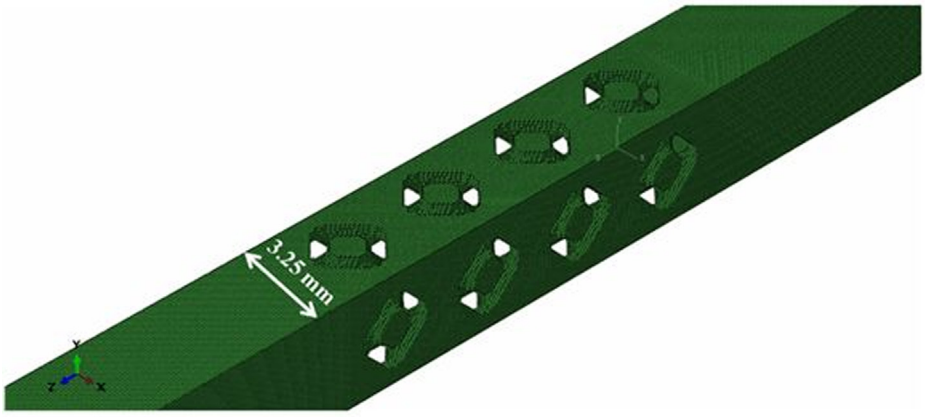

a)

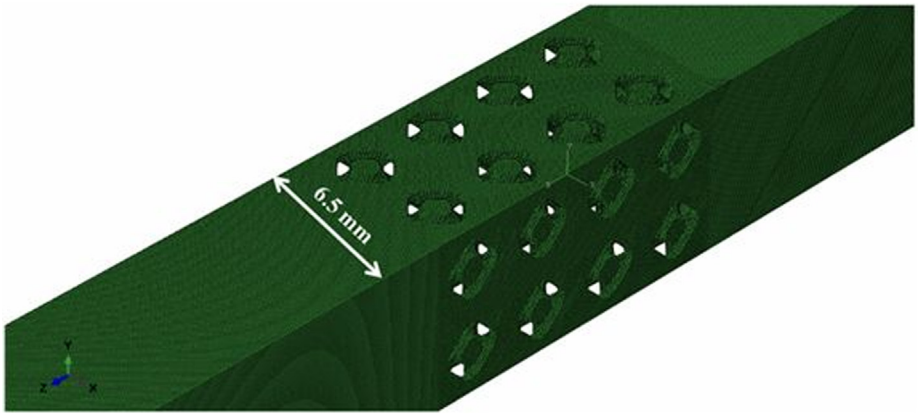

b)

Fig. 2. Computational SP models: Periodic model (a) and Symmetric model (b).

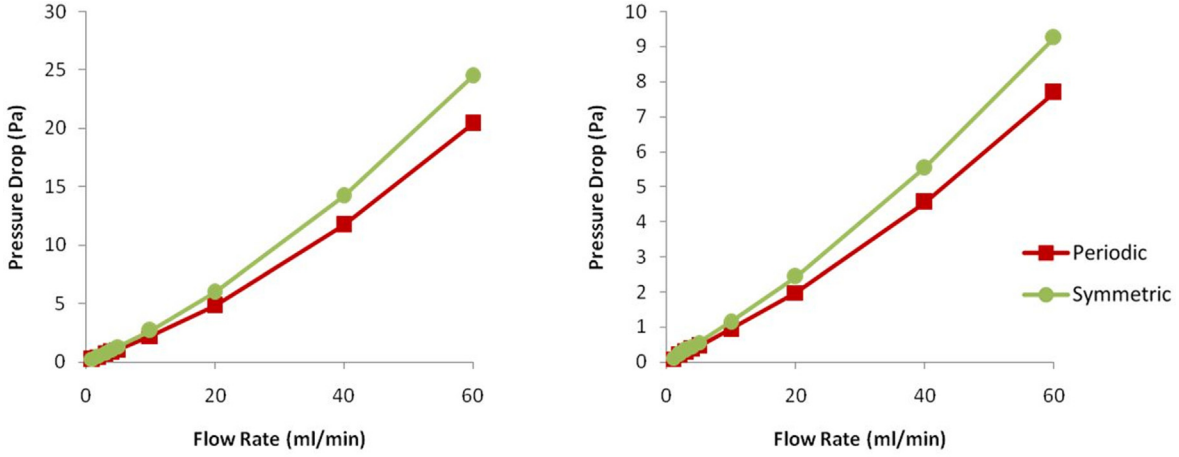

a) b)

Fig. 3. Calculated pressure drop in function of the flow rate for the periodic and symmetric CFD models: SP60 (a) and SP70 (b).

Table 1
Pressure drop (Pa) as a function of the flow rate for the experimental and corrected CFD periodic values.

Geometry		Inlet flow rate (ml/min)				
		5	10	20	40	60
SP60	Numerical	1.28	2.64	5.79	14.09	24.51
	Experimental	3.04 ± 0.56	6.54 ± 1.03	16.16 ± 2.08	42.24 ± 4.98	72.98 ± 5.93
SD60	Numerical	1.45	2.90	5.84	11.95	18.48
	Experimental	5.39 ± 0.99	10.81 ± 2.08	22.21 ± 4.53	49.34 ± 11.38	80.32 ± 17.84
SG60	Numerical	0.79	1.59	3.21	6.66	10.57
	Experimental	2.33 ± 0.42	4.87 ± 1.06	13.94 ± 0.70	32.92 ± 2.44	62.74 ± 2.22
SP70	Numerical	0.55	1.12	2.37	5.46	9.23
	Experimental	1.81 ± 0.20	3.61 ± 0.68	8.16 ± 1.21	20.96 ± 3.48	39.27 ± 11.24
SD70	Numerical	0.91	1.82	3.65	7.45	11.48
	Experimental	3.21 ± 0.56	6.66 ± 1.30	13.54 ± 2.60	30.47 ± 6.16	49.26 ± 11.54
SG70	Numerical	0.53	1.07	2.15	4.46	7.07
	Experimental	1.31 ± 0.35	2.51 ± 0.66	5.43 ± 1.06	11.52 ± 2.91	19.51 ± 5.24

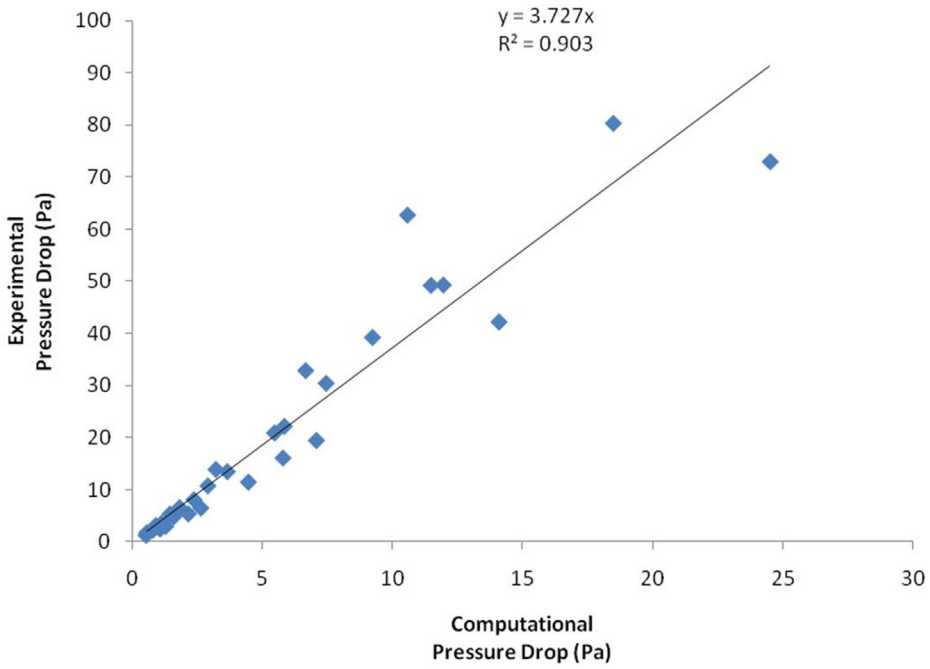

Fig. 4. Correlation between the pressure drop calculated from computational and experimental tests.

can only be used if the scaffold has two symmetry axes in its middle (in the xz and yz planes), which means that it cannot be used for the SG or SD scaffolds, only the SP scaffolds. Nevertheless, these models can be utilised to estimate the approximate effect of the chamber wall, to be applied to all the periodic models.

2.3. Permeability calculation

After obtaining the pressure difference between the ends of the permeability chamber, the scaffold's permeability can be calculated using Darcy's Law (Jones, 1962):

$$K = \frac{Q * \mu * L}{A * \Delta P} \quad (1)$$

In this equation, K is the permeability (m^2); ΔP is the pressure drop measured between the entrance and the exit of the permeability chamber (Pa); L is the length of the scaffold (m); A is the cross sectional area of the scaffold (m^2); μ is the dynamic viscosity of the fluid (Pa.s) and Q is the inlet flow rate (m^3/s). It should be highlighted that the pressure drop in this equation is not the measured value, but instead the difference between the values measured with and without a scaffold. In other words, before calculating the permeability of a scaffold, it is first necessary to determine the baseline pressure drop of the empty setup (experimental and numerically). Furthermore, the implementation of Darcy's law is better indicated for Reynolds numbers up to 1 (Chor and Li, 2007; Ochoa et al., 2008), which occur at relatively low flow rates. Taking this into consideration, alongside the fact that optimal mineralization for bone tissue normally occurs at flow rates below 10 ml/min according to the literature (Chor and Li, 2007; Mccoy et al., 2012; Zhao et al., 2018), this work only employs the calculation of Darcy's permeability for flow rates between 1 and 5 ml/min. Having that the experimental flow rate range is from 5 to 60 ml/min, permeability here is calculated with the computational output, by averaging the pressure drop from 1 to 5 ml/min.

3. Results

Fig. 3 shows the computed pressure drop for the two SP scaffolds, for each model, as a function of the increasing flow rate. This comparison shows that the values from the symmetric models were 18% to 22% higher than the periodic models, with an average

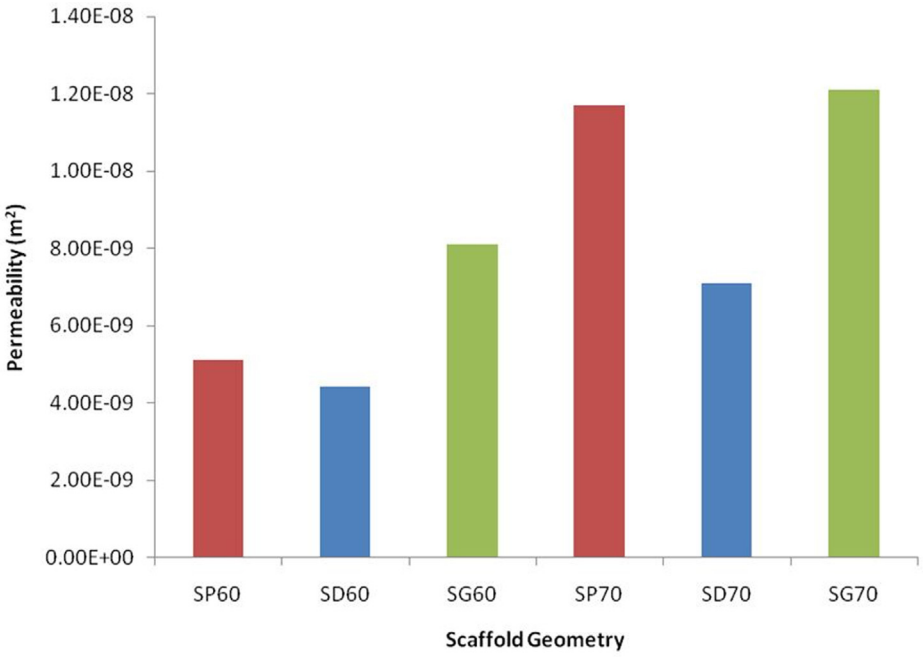

Fig. 5. Average calculated permeability (from 1 to 5 ml/min) from the corrected CFD periodic models for all scaffolds.

of 20%. This value was the result of the effect of the chamber wall on the SP scaffolds (seeing as the chamber wall is the significant difference between the two models). Taking this into consideration, this effect of an increase in the pressure drop of 20% was applied to the six periodic models (by multiplying all the calculated permeabilities by a correction factor of 1.2, which was calculated from the 20%).

After establishing the correction factor to apply to all periodic models, a comparison was made between the pressure drop of corrected numerical models and the experimental data, in order to validate the numerical models (Table 1). This comparison reveals that all the experimental pressure drop values are significantly higher than the numerical values. The experimental results are, on average, four times higher than the numerical outputs. In order to determine whether these two sets of permeability values have a good correlation, a comparison was established between the two sets (Fig. 4). This comparison revealed a R^2 equal to 0.903, indicating high correlation between the numerical and experimental values.

Afterwards, an average permeability of the scaffolds was calculated using Darcy's law (Equation (1)) on the numerical pressure drops values (Fig. 5). Because of the previously established limitations of Darcy's law, only pressure drops calculated from flow rates lower than or equal to 5 ml/min were used in this calculation.

Subsequently, the fluid flow streamlines were analysed in order to better understand how the cells might interact with the scaffold. This is because fluid streamlines highlight the cell trajectory through a scaffold, allowing the analysis of which scaffold geometry best promotes the interaction between cells and the scaffold wall (Campos Marín et al., 2017). The streamlines also illustrate how differences in the inlet flow rate affect the cell's trajectory.

Fig. 6 shows the velocity magnitude and the fluid streamlines from the side and outlet of each of the three scaffolds. These streamlines reveal an almost straight path for the SP scaffolds, squared helixes for the SD scaffolds and circular helixes for the SG scaffold.

Fig. 7 shows an example of the velocity magnitude and the fluid streamlines of the SP scaffold when varying the inlet flow rate. The higher the inlet flow rate is, the less volume is occupied by the streamlines inside the scaffold.

4. Discussion

The computational approach presented in this work revealed to be effective to determine the permeability of TPMS scaffolds. However, some assumptions were made to overcome the computational complexity of the problem. From the two alternative models, the symmetric approach is the one that more accurately reflect the actual scaffolds inside the permeability chamber. This is because the symmetric models take into account the permeability chamber wall, causing an increase in the measured pressure, unlike the periodic models. However, the conditions required to employ the symmetric boundary are met only for the SP scaffolds. Nevertheless, by applying the correction factor of 1.2 in order to include the effects of the chamber wall, the periodic models can be used instead of the complete scaffold model. When comparing the pressure differences obtained from the symmetric model to the periodic model with the correction factor, they are almost identical, with the error between the two always between 0% and 3%. This indicates how the periodic model with a correction factor of 1.2 is a good approximation for SP permeability simulations. However, without any simulations conducted with a complete model for either the SD or SG scaffolds, the correction factor for both geometries might be slightly different than the 1.2 factor for the SP.

The normalized permeability values calculated by (Montazerian et al., 2017) have shown that, for similar porosities, the SG geometries always had a higher permeability than the SD geometries; the SP scaffolds were less permeable than the SD scaffolds at low porosities but were more permeable at higher porosities. At high porosities, the permeability values of the SP scaffolds were very close to the permeability values of the SG scaffolds. These tendencies were also observed in the periodic models of the present work (for 70% porosity the SP and SG scaffold presented very similar permeability at $11.7*10^{-9}$ mm^2 and $12.1*10^{-9}$ mm^2, respectively),

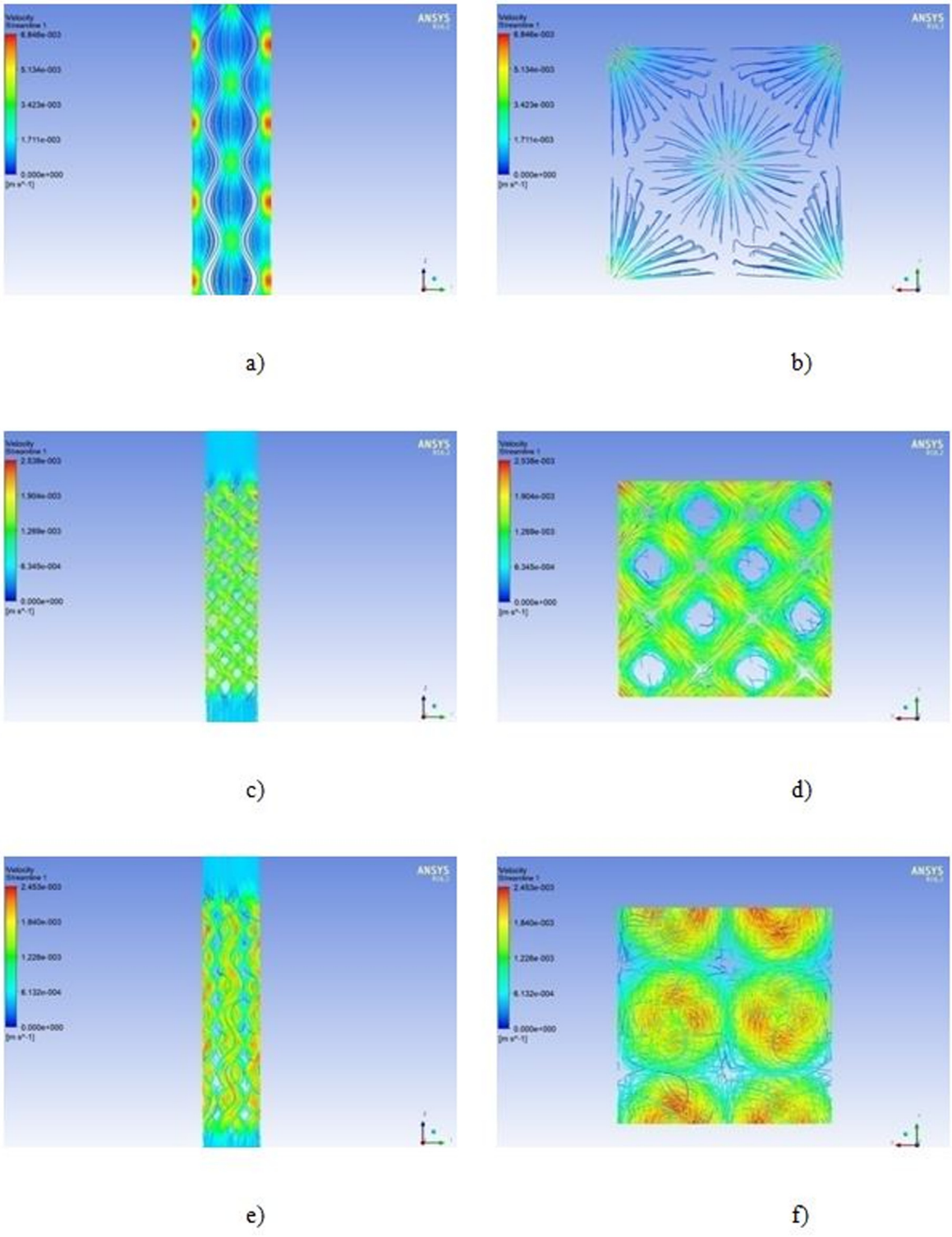

Fig. 6. Streamlines within the scaffolds, with a 5 ml/min inlet flow rate: SP70 side view (a); SP70 outlet view (b); SD70 side view (c); SD70 outlet view (d); SG70 side view (e); SG70 outlet view (f).

which strengthen the validity of the results obtained on the CFD simulations. The correlation between the calculated and measured permeability values (R^2 = 0.903, with an offset of four times) was close to what was determined by Dias et al. (2012) (R^2 = 0.9172, with a similar magnitude offset). This seems to confirm that: i) the models are indeed limited by not including factors such as roughness and wettability surface effects of the materials; ii) the numerical models still accompany the experimentally captured permeability evolution.

Additionally, it is known that simulated and manufactured geometries may be different to a certain extent, due to small imperfections in the 3D printing process (Campos Marin and Lacroix, 2015; Castro et al., 2019b; Santos et al., 2020): there is no way to warrant that the support wax is completely removed

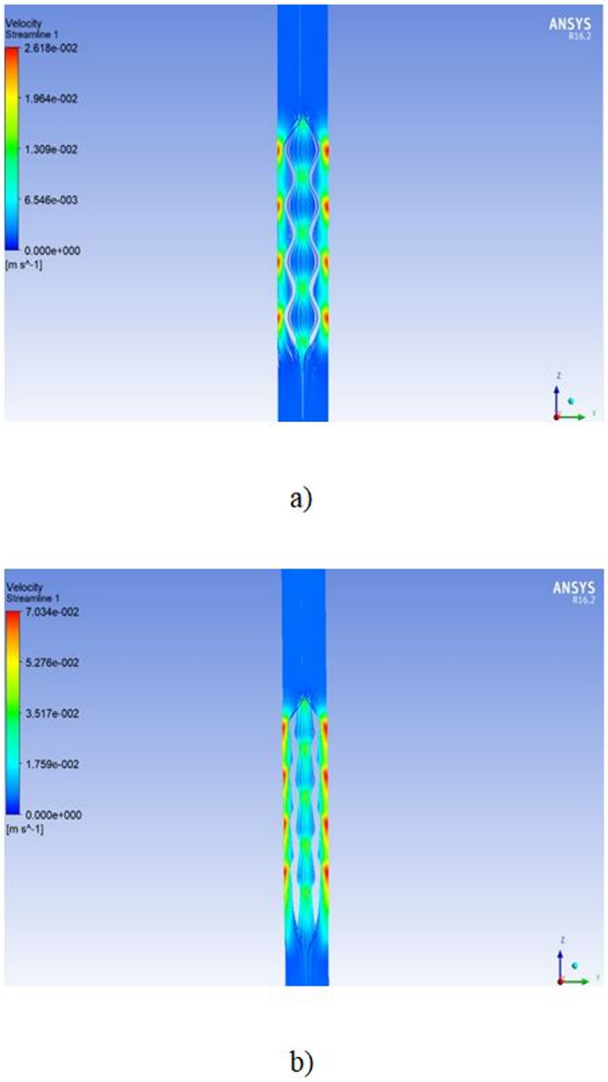

Fig. 7. Sideview of SP70 streamlines as a function of the inlet flow rate: 20 ml/min (a) and a 60 ml/min (b).

from inside the scaffolds, given the nature of this manufacturing process. This may cause blockages to the fluid flow, but previous studies have shown that the alterations in geometry (and subsequent decrease in permeability) shall be limited (Castro et al., 2019b).

As expected, the periodic models revealed how, for the same geometry, a lower porosity results in a lower permeability. However, when comparing different geometries, a lower porosity was not an assurance of a lower permeability. An example of this is how the SG60 has a higher permeability than the SD70 even though it has a lower porosity. The outputs support the view that even though porosity is the main factor in determining a scaffold's permeability, its curvature also plays an important role. This means that geometry needs to be considered alongside porosity when one is designing a TPMS scaffold for a particular BTE application. The curvature is also important because the differentiation of cells inside a scaffold is dependent on the velocity of the fluid passing through them and the shear strain they are subjected to (Castro and Lacroix, 2018). Therefore, being able to control a scaffold's permeability would allow a more precise control (or prediction) of the differentiation of cells inside the scaffold, having that both shear stress and fluid velocity are related to permeability.

The streamlines obtained in the CFD analysis showed that, for each model, there is not a single path for fluid permeation, but several paths with the same shape. These paths are dependent on the geometry of the scaffold: linear paths that expand in the interconnected areas for the SP scaffolds; circular helixes for the SG scaffolds and squared helixes for the SD scaffolds. Even though there are zones of connection between these paths, they never combine or separate, meaning that the number of paths is consistent throughout the scaffold.

Further analysis of streamlines demonstrated how the SP scaffolds were the only ones where there were large non-permeated volumes, indicating that when proceeding to cell seeding, the cells would not be propelled into these areas (Campos Marin et al., 2017). The volumes were the paths could have merged, which were perpendicular to the fluid flow, presented an appealing zone where the cells could be deposited and differentiated. However, if the flow does not pass through these zones, there will be a smaller area of interaction between the scaffold walls and cells. Whether the curvature of those areas promotes cell differentiation or not (Blanquer et al., 2017; Egan et al., 2018; Guyot et al., 2016) is irrelevant if there isn't cell seeding. This problem was worse at higher inlet flow rates where less volume is occupied by the streamlines inside the scaffold. All of this ends in a further decrease in the interaction between the cells and the scaffold, and a longer permeability chamber is required for the fluid flow to stabilize, making the SP geometry less desirable as a possible scaffold design.

In the end, the problem raised regarding the SP scaffolds stem from its design, i.e., straight channels connected between them that severally minimize the cell-scaffold interaction. The fact the flow is not forced into any change of directions and being able to travel in an almost straight line, means that the cells might pass the scaffold without interacting with it at all, rendering the entire purpose of the scaffold moot. However, the other two TPMS geometries, with more complex internal curvatures, did not present this impediment. While both present paths that force the interaction between the flow and the scaffold walls, the design of the SD geometries causes the lowest permeability of all scaffolds. This means the most advisable scaffold choice for most BTE applications, that has both a high permeability and a travel path that leads the cells inside the flow to interact with the scaffold, is the SG geometry. Nevertheless, the SD scaffolds presented the most stable permeability out of the three scaffolds regarding the increase in inlet flow rate (making it the most consist geometry). This means that the decrease in permeability for higher inlet flow rates was minimal for these scaffolds. Therefore, SD scaffolds might be the preferable design in scenarios which involve fluids travelling at varying velocities and that have a need for a constant permeability.

To sum up, this study was able to establish a good correlation between the numerical models and the experimental setup towards the determination of the permeability of these TPMS scaffolds, which was poorly explored in previous studies. It was confirmed that higher porosities did not necessarily mean a higher permeability. This implies that the scaffold geometry and intrinsically their internal curvature need to be considered alongside porosity when designing BTE scaffolds. As so the outcomes of this study show how SP designs are inadequate in comparison with SG scaffolds, if one is looking for a fluid-driven favourable environment for cell seeding and proliferation. The numerical-experimental discrepancies might have been caused by either the simplifications that were considered for the numerical model or the inherent imprecisions to the experimental method, which will be explored in further studies. Additionally, future work will consider different testing conditions and cell seeding assays.

Acknowledgments

This research was funded by Portuguese Science and Technology Foundation, through IDMEC, under LAETA project UIDB/50022/2020 and also through project PTDC/BBB-BMC/5655/2014.

References

3D Systems, 2017. MultiJet Plastic Printers VisiJet ® M3 Advanced Plastics. Rock Hill, USA.

Ali, D., Sen, S., 2018a. Computational Fluid Dynamics Study of the Effects of Surface Roughness on Permeability and Fluid Flow-Induced Wall Shear Stress in Scaffolds. Ann. Biomed. Eng. 46, 2023–2035. https://doi.org/10.1007/s10439-018-2101-z.

Ali, D., Sen, S., 2018b. Permeability and fluid flow-induced wall shear stress of bone tissue scaffolds: Computational fluid dynamic analysis using Newtonian and non-Newtonian blood flow models. Comput. Biol. Med. 99, 201–208. https://doi.org/10.1016/j.compbiomed.2018.06.017.

Blanquer, S.B.G., Werner, M., Hannula, M., Sharifi, S., Lajoinie, G.P.R., Eglin, D., Hyttinen, J., Poot, A.A., Grijpma, D.W., 2017. Surface curvature in triply-periodic minimal surface architectures as a distinct design parameter in preparing advanced tissue engineering scaffolds. Biofabrication 9. https://doi.org/10.1088/1758-5090/aa6553.

Campos Marín, A., Brunelli, M., Lacroix, D., 2017. Flow perfusion rate modulates cell deposition onto scaffold substrate during cell seeding. Biomech. Model. Mechanobiol. https://doi.org/10.1007/s10237-017-0985-4

Campos Marin, A., Grossi, T., Bianchi, E., Dubini, G., Lacroix, D., 2017. μ-Particle tracking velocimetry and computational fluid dynamics study of cell seeding within a 3D porous scaffold. J. Mech. Behav. Biomed. Mater. 75, 463–469. https://doi.org/10.1016/j.jmbbm.2017.08.003.

Campos Marin, A., Grossi, T., Bianchi, E., Dubini, G., Lacroix, D., 2016. 2D μ-Particle Image Velocimetry and Computational Fluid Dynamics Study Within a 3D Porous Scaffold. Ann. Biomed. Eng. 45, 1341–1351. https://doi.org/10.1007/s10439-016-1772-6.

Campos Marin, A., Lacroix, D., 2015. The inter-sample structural variability of regular tissue-engineered scaffolds significantly affects the micromechanical local cell environment 20140097 20140097 Interface Focus 5. https://doi.org/10.1098/rsfs.2014.0097.

Castro, A.P.G., Lacroix, D., 2018. Micromechanical study of the load transfer in a polycaprolactone–collagen hybrid scaffold when subjected to unconfined and confined compression. Biomech. Model. Mechanobiol. 17, 531–541. https://doi.org/10.1007/s10237-017-0976-5.

Castro, A.P.G., Pires, T., Santos, J., Gouveia, B.P., Fernandes, P.R., 2019a. Permeability versus Design in TPMS Scaffolds. Materials (Basel). 12, 1313. https://doi.org/10.3390/ma12081313.

Castro, A.P.G., Ruben, R.B., Gonçalves, S.B., Pinheiro, J., Guedes, J.M., Fernandes, P.R., 2019b. Numerical and experimental evaluation of TPMS Gyroid scaffolds for bone tissue engineering. Comput. Methods Biomech. Biomed. Engin. 22, 567–573. https://doi.org/10.1080/10255842.2019.1569638.

Chen, L., Song, W., Markel, D.C., Shi, T., Muzik, O., Matthew, H., Ren, W., 2016. Flow perfusion culture of MC3T3-E1 osteogenic cells on gradient calcium polyphosphate scaffolds with different pore sizes. J. Biomater. Appl. 30, 908–918. https://doi.org/10.1177/0885328215608335.

Chor, M.V., Li, W., 2007. A permeability measurement system for tissue engineering scaffolds. Meas. Sci. Technol. 18, 208–216. https://doi.org/10.1088/0957-0233/18/1/026.

Coelho, P.G., Hollister, S.J., Flanagan, C.L., Fernandes, P.R., 2015. Bioresorbable scaffolds for bone tissue engineering: Optimal design, fabrication, mechanical testing and scale-size effects analysis. Med. Eng. Phys. 37, 287–296. https://doi.org/10.1016/j.medengphy.2015.01.004.

Daish, C., Blanchard, R., Pirogova, E., Harvie, D.J.E., Pivonka, P., 2019. Numerical calculation of permeability of periodic porous materials: Application to periodic arrays of spheres and 3D scaffold microstructures. Int. J. Numer. Methods Eng. 118, 783–803. https://doi.org/10.1002/nme.6037.

Dias, M.R., Fernandes, P.R., Guedes, J.M., Hollister, S.J., 2012. Permeability analysis of scaffolds for bone tissue engineering. J. Biomech. 45, 938–944. https://doi.org/10.1016/j.jbiomech.2012.01.019.

Egan, P.F., Gonella, V.C., Engensperger, M., Ferguson, S.J., Shea, K., 2017. Computationally designed lattices with tuned properties for tissue engineering using 3D printing. PLoS One 12, 1–20. https://doi.org/10.1371/journal.pone.0182902.

Egan, P.F., Shea, K.A., Ferguson, S.J., 2018. Simulated tissue growth for 3D printed scaffolds. Biomech. Model. Mechanobiol. 17, 1481–1495. https://doi.org/10.1007/s10237-018-1040-9.

Giannitelli, S.M., Accoto, D., Trombetta, M., Rainer, A., 2014. Current trends in the design of scaffolds for computer-aided tissue engineering. Acta Biomater. 10, 580–594. https://doi.org/10.1016/j.actbio.2013.10.024.

Guyot, Y., Papantoniou, I., Luyten, F.P., Geris, L., 2016. Coupling curvature-dependent and shear stress-stimulated neotissue growth in dynamic bioreactor cultures: a 3D computational model of a complete scaffold. Biomech. Model. Mechanobiol. 15, 169–180. https://doi.org/10.1007/s10237-015-0753-2.

Hollister, S.J., Flanagan, C.L., Zopf, D.A., Morrison, R.J., Nasser, H., Patel, J.J., Ebramzadeh, E., Sangiorgio, S.N., Wheeler, M.B., Green, G.E., 2015. Design Control for Clinical Translation of 3D Printed Modular Scaffolds. Ann. Biomed. Eng. 43, 774–786. https://doi.org/10.1007/s10439-015-1270-2.

Jones, K.R., 1962. On the differential form of Darcy's law. J. Geophys. Res. 67, 731–732. https://doi.org/10.1029/JZ067i002p00731.

Kapfer, S.C., Hyde, S.T., Mecke, K., Arns, C.H., Schröder-Turk, G.E., 2011. Minimal surface scaffold designs for tissue engineering. Biomaterials 32, 6875–6882. https://doi.org/10.1016/j.biomaterials.2011.06.012.

Kelly, C.N., Miller, A.T., Hollister, S.J., Guldberg, R.E., Gall, K., 2017. Design and Structure-Function Characterization of 3D Printed Synthetic Porous Biomaterials for Tissue Engineering. Adv. Healthc. Mater. 1701095, 1701095. https://doi.org/10.1002/adhm.201701095.

Maskery, I., Sturm, L., Aremu, A.O., Panesar, A., Williams, C.B., Tuck, C.J., Wildman, R. D., Ashcroft, I.A., Hague, R.J.M., 2018. Insights into the mechanical properties of several triply periodic minimal surface lattice structures made by polymer additive manufacturing. Polymer (Guildf). 152, 62–71. https://doi.org/10.1016/j.polymer.2017.11.049.

Mccoy, R.J., Jungreuthmayer, C., O'Brien, F.J., 2012. Influence of flow rate and scaffold pore size on cell behavior during mechanical stimulation in a flow perfusion bioreactor. Biotechnol. Bioeng. 109, 1583–1594. https://doi.org/10.1002/bit.24424.

Melchels, F.P.W., Barradas, A.M.C., van Blitterswijk, C.A., de Boer, J., Feijen, J., Grijpma, D.W., 2010. Effects of the architecture of tissue engineering scaffolds on cell seeding and culturing. Acta Biomater. 6, 4208–4217. https://doi.org/10.1016/j.actbio.2010.06.012.

Melchels, F.P.W., Tonnarelli, B., Olivares, A.L., Martin, I., Lacroix, D., Feijen, J., Wendt, D.J., Grijpma, D.W., 2011. The influence of the scaffold design on the distribution of adhering cells after perfusion cell seeding. Biomaterials 32, 2878–2884. https://doi.org/10.1016/j.biomaterials.2011.01.023.

Montazerian, H., Zhianmanesh, M., Davoodi, E., Milani, A.S., Hoorfar, M., 2017. Longitudinal and radial permeability analysis of additively manufactured porous scaffolds: Effect of pore shape and porosity. Mater. Des. 122, 146–156. https://doi.org/10.1016/j.matdes.2017.03.006.

Nasrollahzadeh, N., Pioletti, D.P., 2016. Experimental method to characterize the strain dependent permeability of tissue engineering scaffolds. J. Biomech. 49, 3749–3752. https://doi.org/10.1016/j.jbiomech.2016.09.021.

Ochoa, I., García-Aznar, J.M., Boccaccini, A.R., Doblaré, M., Sanz-Herrera, J.A., Yunos, D.M., 2008. Permeability evaluation of 45S5 Bioglass®-based scaffolds for bone tissue engineering. J. Biomech. 42, 257–260. https://doi.org/10.1016/j.jbiomech.2008.10.030.

Porter, J.R., Ruckh, T.T., Popat, K.C., 2009. Bone tissue engineering: A review in bone biomimetics and drug delivery strategies. Biotechnol. Prog. 25, 1539–1560. https://doi.org/10.1002/btpr.246.

Rahbari, A., Montazerian, H., Davoodi, E., Homayoonfar, S., 2017. Predicting permeability of regular tissue engineering scaffolds: scaling analysis of pore architecture, scaffold length, and fluid flow rate effects. Comput. Methods Biomech. Biomed. Engin. 20, 231–241. https://doi.org/10.1080/10255842.2016.1215436.

Santos, J., Pires, T., Gouveia, B.P., Castro, A.P.G., Fernandes, P.R., 2020. On the permeability of TPMS scaffolds. J. Mech. Behav. Biomed. Mater. 110,. https://doi.org/10.1016/j.jmbbm.2020.103932 103932.

Shi, J., Zhu, L., Li, L., Li, Z., Yang, J., Wang, X., 2018. A TPMS-based method for modeling porous scaffolds for bionic bone tissue engineering. Sci. Rep. 8. https://doi.org/10.1038/s41598-018-25750-9.

Szklanny, A.A., Debbi, L., Merdler, U., Neale, D., Muñiz, A., Kaplan, B., Guo, S., Lahann, J., Levenberg, S., 2019. High-Throughput Scaffold System for Studying the Effect of Local Geometry and Topology on the Development and Orientation of Sprouting Blood Vessels. Adv. Funct. Mater. https://doi.org/10.1002/adfm.201901335

Webber, M.J., Khan, O.F., Sydlik, S.A., Tang, B.C., Langer, R., 2015. A perspective on the clinical translation of scaffolds for tissue engineering. Ann. Biomed. Eng. 43, 641–656. https://doi.org/10.1007/s10439-014-1104-7.

Yoo, D., 2012. New paradigms in internal architecture design and freeform fabrication of tissue engineering porous scaffolds. Med. Eng. Phys. 34, 762–776. https://doi.org/10.1016/j.medengphy.2012.05.008.

Zhao, F., van Rietbergen, B., Ito, K., Hofmann, S., 2018. Flow rates in perfusion bioreactors to maximise mineralisation in bone tissue engineering in vitro. J. Biomech. 79, 232–237. https://doi.org/10.1016/j.jbiomech.2018.08.004.

Zhianmanesh, M., Varmazyar, M., Montazerian, H., 2019. Fluid Permeability of Graded Porosity Scaffolds Architectured with Minimal Surfaces. ACS Biomater. Sci. Eng. 5, 1228–1237. https://doi.org/10.1021/acsbiomaterials.8b01400.